LAWRENCE
LIVERMORE
NATIONAL
LABORATORY

LLNL-JRNL-665313

Calculation of laser absorption by metal powders in additive manufacturing

C. D. Boley, S. A. Khairallah, A. M. Rubenchik

December 11, 2014

Applied Optics

Disclaimer

Calculation of laser absorption by metal powders in additive manufacturing

C. D. Boley,[1,*] S. A. Khairallah,[1] and A. M. Rubenchik[1]

[1]*Lawrence Livermore National Laboratory, Livermore CA 94550*
[*]*Corresponding author:* boley1@llnl.gov

We have calculated the absorption of laser light by a powder of metal spheres, typical of the powder employed in laser powder-bed fusion additive manufacturing. Using ray-trace simulations, we show that the absorption is significantly larger than its value for normal incidence on a flat surface, because of multiple scattering. We investigate the dependence of absorption on powder content (material, size distribution, and geometry), and on beam size.

OCIS codes: (080.2710) Inhomogeneous optical media; (080.5692) Ray trajectories in inhomogeneous media; (160.1245) Artificially engineered materials.

1. Introduction

Additive manufacturing is a fast-growing technology for building the parts of a device [1]. In selective laser melting, the layers of a metal powder are melted in a controlled manner, forming successive slices of a part. This process is characterized by a number of parameters, including the powder material, the layer thickness and porosity, the laser beam size and profile, and the laser scan speed. Reliable process modeling is very useful in order to determine the optimal parameters and to anticipate possible problems in the build process.

An important component of modeling efforts is the description of the absorption of the metal powder and of the spatial distribution of the absorbed radiation. Direct measurements of the absorption are quite difficult [2]. Also it is problematic to make use of measurements obtained without detailed specifications of the experiment, since the absorption depends on the parameters noted above, along with the distribution of particle sizes and the spatial distribution of the particles. Thus it is not sufficient to know the results for one particular powder of a given material and for a particular beam, as we demonstrate below. Similarly, the spatial distribution of absorbed radiation is difficult to obtain experimentally. These considerations reinforce the usefulness of absorption calculations.

A commonly used laser absorption model, proposed in [3], assumes diffusive radiation transport in the powder. This assumption, however, is not applicable for the thin, low-porosity metal powder layer used in the selective laser melting process, for which the thickness is a few powder particles. As we shall see, in this case the energy is typically absorbed in the top layer, and the absorption is highly non-uniform. These circumstances are inconsistent with a diffusion model.

Physically, the powder is an assembly of metal particles, taken here to be spheres, with sizes appreciably larger than the laser wavelength (taken as about 1 μm) and with a complex refractive index appropriate to the material and the wavelength. It is natural to use ray tracing to calculate the powder absorption. This has previously been considered, e.g., in [4], but the angular and polarization dependence of the absorption of incident rays was neglected.

In the present paper, we report the results of comprehensive absorption modeling, including all the effects mentioned above. A major challenge is the problem of tracing rays within an assembly of thousands of objects, while keeping track of the angle, polarization, power, and reflection/refraction of individual rays. However, this issue has long been the subject of study, and commercial software is available for handling it. Here we utilize the product FRED [5], a multipurpose optics code widely used in optical design and analysis. In our application, which differs from typical applications, we make extensive use of its ray-trace capability. In order to handle our problem, substantial scripting and post-processing was required. Previously, we employed FRED in the similar problem of laser interactions with composite materials [6].

To begin the calculations, we consider a powder consisting of spheres of a single size, densely packed in a hexagonal structure. Six materials (Ag, Al, Au, Cu, stainless steel, and Ti) are considered. We first study the overall absorptivity of such a powder, by assuming a uniform beam of width large compared with the particle size, so that the absorption is nearly independent of the beam position. The calculations show that the resulting powder absorptivity is significantly higher than the absorptivity of a flat surface or of a single, isolated sphere, thus confirming the important role of multiple scattering. We demonstrate that most of the energy is absorbed in the top layer of the array.

A real powder has a distribution of sizes and is not densely packed. Therefore we use a particle-packing program [7] to set up a powder layer. The algorithm is similar to that of the rain-packing model [8]. Specific calculations are performed for two powders. The first powder is that used in the Concept Laser M2 metal powder-bed fusion additive manufacturing machine [9]. Some experimental results obtained recently at LLNL with this device are described in [10]. For some specific calculations we use the parameters from these experiments. For the second powder, we consider a bimodal particle distribution that provides a higher powder packing density. We demonstrate that this can lead to a significant increase in the powder absorption, especially for highly reflective materials.

For a laser beam width comparable with the typical powder sphere size (a typical situation for the Concept Laser machine), the absorption is sensitive to the beam position. Calculating the absorption pattern along a track through the powder, we show that the absorption fluctuates noticeably along the path on a distance scale appreciably larger than the particle size.

Finally, we summarize the results and discuss their impact on the additive manufacturing process.

2. Absorptivity and ray tracing calculations

In practical applications, the typical particle radius (generally at least 10 μm) appreciably exceeds the laser wavelength, and ray tracing is applicable for the description of the interaction. For a beam striking the surface of a dielectric material at an angle θ to the normal, the absorptivity is given by the Fresnel formulas [11]:

$$\alpha_s(\theta) = 1 - \left| \frac{\cos\theta - (n^2 - \sin^2\theta)^{1/2}}{\cos\theta + (n^2 - \sin^2\theta)^{1/2}} \right|^2 , \tag{1}$$

$$\alpha_p(\theta) = 1 - \left| \frac{n^2\cos\theta - (n^2 - \sin^2\theta)^{1/2}}{n^2\cos\theta + (n^2 - \sin^2\theta)^{1/2}} \right|^2 , \tag{2}$$

in which the electric field is either perpendicular (S) or parallel (P) to the plane of incidence, and n is the complex index of refraction of the material (divided by the index of refraction of the external medium, which we take as unity). A general polarization can be expressed as a combination of S and P.

Figure 1 shows the absorptivity of stainless steel, which has a refractive index $n = 3.27 + 4.48i$ at a wavelength of 1 μm [12], as a function of the incident angle. At perpendicular incidence, the absorptivity of each polarization is about 0.34. As the angle is increased, the absorptivity decreases smoothly for S polarization, while it increases to a maximum of about 0.75 at 80 deg for P polarization. The absorptivity is greater in the latter case because the electric field has a component directed into the material.

For a large, uniform beam incident upon an isolated sphere, the absorptivity can readily be calculated and has the pattern shown in Figure 2. In this case, the angle and the power split between S and P depend on the point of incidence on the sphere.

In our ray-tracing, a ray is tracked from surface to surface. It has a particular power in each polarization state. After an interaction, the reflected ray either strikes a neighboring surface (sphere or substrate), or exits the system. In the former case, the refracted ray deposits power within the sphere or substrate, and this deposited power is not followed. After every reflection, therefore, the power of a ray decreases. We stop propagation of a ray when its power drops below 0.1% of its initial power. The number of rays varied from 50 000 to a few million, depending on the specific problem. This number was always chosen sufficiently high so that the results were insensitive to the specific choice.

3. Ideal powder array

We now turn to a powder of identical spheres, assuming ideal packaging, i.e. hexagonal close-packing. We consider two layers of spheres, resting on a substrate of the same material. This is similar to the actual setup in laser powder-bed fusion additive manufacturing. Calculations of the absorptivity were performed for several metals, illuminated perpendicularly from above, as shown in Fig. 3. The refractive indices near a wavelength of 1 μm were taken from a data compilation [12].

First, calculations were performed for a uniform circular beam having a radius much larger than the radius of a sphere. The results, which clearly are independent of the particular sizes, are summarized in Table 1. Most important for each metal is the total absorptivity by the spheres and the substrate (column 9). This is to be

Table 1. Absorption Details (α denotes the absorptivity)

(1) Material	(2) Re(n)	(3) Im(n)	(4) α (flat surface)	(5) α (isolated sphere)	(6) α (top layer)	(7) α (bottom layer)	(8) α (substrate)	(9) α (spheres + substrate)	(10) α (spheres + substrate)/ α (flat surface)
Ag	0.23	7.09	0.018	0.020	0.072	.047	0.010	0.13	7.2
Al	1.244	10.	0.047	0.056	0.15	0.063	0.011	0.22	4.7
Au	0.278	7.20	0.021	0.024	0.081	0.050	0.011	0.14	6.7
Cu	0.35	6.97	0.028	0.032	0.101	0.055	0.011	0.17	6.1
SS	3.27	4.48	0.34	0.36	0.53	0.062	0.013	0.60	1.7
Ti	3.45	4.	0.38	0.40	0.56	0.062	0.014	0.64	1.7

compared with the absorptivity of the metal at normal incidence on a flat surface (column 4), and the average absorptivity of an isolated sphere illuminated by a uniform beam (column 5).

Note that the most of the power is absorbed in the top layer of the spheres (column 6). Little more than 1% of the power penetrates beneath the two layers to the substrate (column 8).

We see that the total absorptivity of the spheres is noticeably higher than either the normal-incidence value or the single-sphere value. This effect has observed in experiment [2]. The enhancement is due to multiple scattering, as illustrated in Fig. 4. A ray can scatter repeatedly, leading to additional absorption relative to the case of a flat surface. Thus the relative increase in absorptivity is higher for highly reflective metals (Ag, Al, Au, Cu) than for moderately absorbing metals (SS and Ti). In the former case, this ratio (column 10) varies from 4.7 to 7.2, while in the latter case, the ratio decreases to 1.7.

More generally, one is interested in not only the total absorbed power but also the spatial distribution of the absorbed power. In some additive manufacturing machines, the laser beam size is roughly comparable to the powder particle size. Here we consider a powder with spheres of radius 10 μm and a beam having a $1/e^2$ radius of 24 μm. From now on, the radius of a Gaussian beam always refers to the $1/e^2$ radius.

Figure 5 shows the distribution of absorbed irradiance along the top layer of a stainless steel array, as the beam is rapidly scanned across the array. This distribution was obtained by calculating the absorbed irradiance patterns at a number of points along the path, and taking the average. It gives a qualitative picture of the absorbed irradiance on a time scale short compared to thermal-mechanical times, i.e. for a sufficiently fast scanning speed. We see that the scattered light is well confined and that the typical absorption area is comparable to the beam area.

The absorptivity is sensitive to the beam size, and fluctuations of the absorptivity are smoothed with increasing beam size. As shown in Fig. 6, the absorption fluctuates by about 20% for a Gaussian beam of radius 8 μm (80% of the particle radius), and by less than 0.1% when the radius is increased to 24 μm. The fluctuations become negligible for a beam radius of about twice the particle radius. Nevertheless, even in this case the distribution of absorbed power upon a single sphere is very non-uniform.

4. Realistic powder array

A realistic powder has a distribution of sizes and a non-uniform geometrical arrangement, generally with a porosity greater than that of an ideal array.

To generate the powder geometry, we used a particle packing program [7] with an algorithm similar to that of the rain model for random deposition [8]. The program randomly places powder particles, with a specified distribution of sizes, on a powder bed, up to the first contact with other particles or with the substrate. If the contact is with a particle, the particle is randomly perturbed, in an effort to achieve the minimum potential energy due to gravity. Finally, to simulate the removal of extra powder by a coater blade, the program inserts a plane at a specified distance from the substrate and removes all particles intersected by the plane or situated above it.

We consider two specific powder types. The first, shown in Fig. 7, mimics the powder used in the Concept Laser machine [9]. The powder has a Gaussian distribution of radii, with an average radius of 13.5 μm, a full width at half maximum equal to 2.3 μm, radial cutoffs at 8.5 μm and 21.5 μm, and a powder thickness of 43 μm [13]. In the absorption calculations, the path of the beam extends along the length of the powder bed, as shown in the figure.

The stainless steel absorption results encountered along the path are shown in Fig. 8. We see that local variations in the powder structure give rise to sizeable fluctuations in the absorption. The fluctuations occur on a scale of about 100 μm, which is much larger than the typical sphere size. The mechanism for the

Table 2. Total absorptivities for selected materials

Material	Ideal array (Table 1)	Gaussian array	Bimodal array
Ag	0.13	0.081	0.14
Au	0.14	0.093	0.16
SS	0.60	0.58	0.63

fluctuations can be seen in the two inserts in Fig. 8. In the left insert, the incident beam has mainly struck small spheres, with larger spheres on the periphery. This results in multiple reflections and an increased absorption. In the right insert, on the other hand, much of the incident power has reached the substrate, producing fewer reflections and a decreased absorption. In detail, the absorption of the spheres alone has an average of about 0.50 with a standard deviation of about 0.07, while the total absorption (spheres plus substrate) has an average of 0.58 with a standard deviation of 0.03. The reason for the decrease in fluctuations of the total is that the contribution from the substrate tends to cancel that from the spheres (the spheres shield the substrate).

For the second example of a powder, shown in Fig. 9, we consider a bimodal distribution characterized by a 7:1 ratio of radii and a volume fraction of small spheres equal to 20%, as discussed in [14]. This powder was chosen because of its high density, or low porosity. Following [14], we consider a large-sphere radius of 42 μm and a powder thickness of 50 μm.

Figure 10 shows the calculated absorption for stainless steel along a 1 mm laser beam path. In this configuration, holes in the powder layer are practically absent. The absorption minima correspond to situations when the beam mainly strikes a large sphere, with much of the light directly reflected (left insert). The largest absorption occurs when the beam strikes a local assembly of small spheres, as seen in the right insert. The difference between these two cases lies in the ratio of the beam size to the size of the irradiated spheres, with a larger ratio offering more opportunity for multiple reflections. As in the previous case, the absorption fluctuates on a distance scale larger than a particle size, or about 100 μm.

Parenthetically, it should be noted that the problem of a powder structure producing a maximum density has been investigated in a number of studies, e.g., [15]. The structure is not completely disordered, since it includes both regular cells and long-distance correlations. It is not known whether such a structure can be reproduced with the packaging algorithm used here.

Returning to the Gaussian and bimodal powders, let us compare the overall results with those for the ideal powder of the previous section. The results are summarized in Table 2. We see that a change in the powder structure can noticeably affect the absorptivity. For a moderately absorbing metal such as stainless steel, the difference is not large, about a few percent. On the other hand, for highly reflective metals such as silver and gold, the variation can be nearly a factor of 2. In these cases, multiple scattering is very important, and the powder geometry affects the total absorptivity.

5. Discussion and Conclusions

We have developed a detailed ray-trace model which can be used to calculate the absorption and energy deposition in a metal powder, starting with the optical parameters of the constituents and the powder structure. We have found that the absorption is substantially increased relative to its flat-surface value because of multiple scattering. The effect is especially important for highly reflective metals, such as those used in the additive manufacturing of jewelry. We demonstrated that, by optimization of the powder layer structure, one can increase the absorption by nearly a factor of 2.

Let us discuss the importance of the localized energy deposition. There are two general issues regarding absorption non-uniformity, one related to the non-uniformity of absorption within a single particle, and the other related to the non-uniformity of absorption on a larger scale given by the final beam size and the local structure of the actual powder.

Consider first the former issue. The time for homogenization of energy absorbed non-uniformly on a sphere with radius R, due to thermal conduction, is $\tau_c = R^2 / D$, where D is the thermal diffusivity of the metal. Another typical time is the time needed to melt the material, or $\tau_m = R H_m / \alpha_0 I$. Here H_m is the melting enthalpy per volume, I is the laser irradiance, and α_0 is the flat-surface absorptivity. For processing steel with a Concept Laser additive manufacturing machine, one has $R \sim 10$ μm, $D \sim 0.04$ cm²/s, $H_m \sim 8$ kJ/cm³, $\alpha_0 \sim 0.3$, and $I \sim 10$ MW/cm². Therefore the thermal diffusion time is about 25 μs, and the melting time is shorter by nearly a factor of 10. This means that non-uniformity of absorption results in only partial melting of the particle. It can be shown that melt penetrates to the substrate more rapidly due to wetting and capillary forces [16]. Un-melted particle pieces can produce residual voids (e.g. between the particle and substrate) and defects.

This result differs from the conventional model [3] that assumes uniform, volumetric deposition. However, for lower intensities and materials with higher thermal conductivity, when the thermal diffusion rapidly homogenizes the temperature within the particle, our deposition model and the model [3] can produce similar results for the same deposited energy.

Regarding the issue of large-scale variability of absorption, we note that non-uniformity on the scale of 100 μm can produce fluctuations of the melt pool size and can explain the track modulation typically observed in experiments, e.g. [10].

In conclusion, the fact that multiple scattering plays an important role means that the absorption value is strongly affected by the size distribution of the powder spheres and their geometrical arrangement. The non-uniformity of energy deposition affects the melt dynamics. Thus control of the powder structure can be an important tool for optimization of the laser powder-bed fusion additive manufacturing process, and ray-trace modeling is an effective method for achieving this control.

Acknowledgments

We would like to thank W. E. King and W. A. Molander for helpful discussions. This work was performed under the auspices of the U.S. Department of Energy by Lawrence Livermore National Laboratory under Contract DE-AC52-07NA27344. This work was funded by the Laboratory Directed Research and Development Program at LLNL under project tracking code 13-SI-002.

References

1. See, e.g., T. Wohlers, "Wohlers Report 2014. 3D Printing and Additive Manufacturing State of the Industry. Annual Worldwide Progress Report," Wohlers Associates, Inc., Fort Collins, Colorado (2014).

2. N. Tolochko *et al.*, "Absorptance of powder materials suitable for laser sintering," Rapid Prototyping Journal **6**,155 (2000).

3. A. V. Gusarov and J.-P. Kruth, "Modelling of radiation transfer in metallic powders at laser treatment," Int. J. Heat Mass Transfer **48**, 3423-3434 (2005).

4. X. C. Wang *et al.*, "Direct selective laser sintering of hard metal powders: experimental study and simulation," Int. J. Adv. Manuf. Technol. **19**, 351-357 (2002).

5. FRED is distributed by Photon Engineering, LLC, Tucson, AZ.

6. C. D. Boley and A. M. Rubenchik, "Modeling of laser interactions with composite materials," Appl. Opt. **52**, 3329-3337 (2013).

7. G. Friedman, "ParticlePack user's manual," Lawrence Livermore National Laboratory, LLNL-SM-458031 (2011).

8. P. Meakin and R. Jullien, "Restructuring effects in the rain model for random deposition," J. Physique **48**, 1651-1662 (1987).

9. Concept Laser GmbH (www.concept-laser.de/en/home.html).

10. W. E. King, H. D. Barth, V. M. Castillo, G. F. Gallegos, J. W. Gibbs, D. E. Hahn, C. Kamath, and A. M. Rubenchik, "Observation of keyhole-mode laser melting in laser powder-bed fusion additive manufacturing," J. Mater. Process. Technol. **214**, 2915–2925 (2014).

11. L. D. Landau, E. M. Lifshitz, and L. P. Pitaevskii, *Electrodynamics of Continuous Media*, 2nd edition, Pergamon Press, 1984.

12. *Handbook of Optical Constants of Solids*, E. D. Palik, ed. (Academic Press, Orlando, FL, 1985).

13. Powder CL 20ES, produced by Concept Laser GmbH (Ref. 9).

14. R. Kelkar, “Effect of metal powder particle-size distribution on surface roughness for CoCrMo parts manufactured via direct metal laser melting (DMLM) process,” Additive Manufacturing with Powder Metallurgy, Orlando, FL (2014).

15. A. B. Hopkins, F. H. Stillinger, and S. Torquato, “Disordered strictly jammed binary sphere packings attain an anomalously large range of densities,” Phys. Rev. E **88**, 022205 (2013).

16. S. A. Khairallah and A. Anderson, "Mesoscopic Simulation Model of Selective Laser Melting of Stainless Steel Powder," J. Mater. Process. Technol. **214**, 2627-2636 (2014).

Figure Captions

1. Absorptivity α of 1 μm light incident on stainless steel.

2. Absorptivity α of a beam by a single sphere of stainless steel. The beam is polarized horizontally. The absorptivity falls to zero near the left edge and right edge, although this is not resolved in the graphic.

3. Typical rays during illumination of the ideal array.

4. Detail of ray trajectories in Fig. 3, showing multiple scattering from spheres.

5. Irradiances (arbitrary scale) for 61 successive beam positions, from lower left to upper right, in steps of 2 μm. The irradiances pertain to the spherical surfaces. A sample beam spot ($1/e^2$ radius) is shown.

6. Spatial variations of the absorption α along the beam path for beams of different radii.

7. Powder with a Gaussian distribution of sizes. The length of the bed is about 1100 μm, and the beam path is indicated.

8. Absorption α as calculated along the beam path for the Gaussian powder of Fig. 7. The material is stainless steel. The inserts show the powder and incident beam size ($1/e^2$) at locations with high absorption (left) and low absorption (right).

9. Powder with a bimodal distribution of sizes. The powder bed and the beam are as in Fig. 7.

10. Absorption α as calculated along the beam path for the bimodal powder of Fig. 9 (stainless steel). The inserts show the powder and incident beam size at locations with low absorption (left) and high absorption (right).

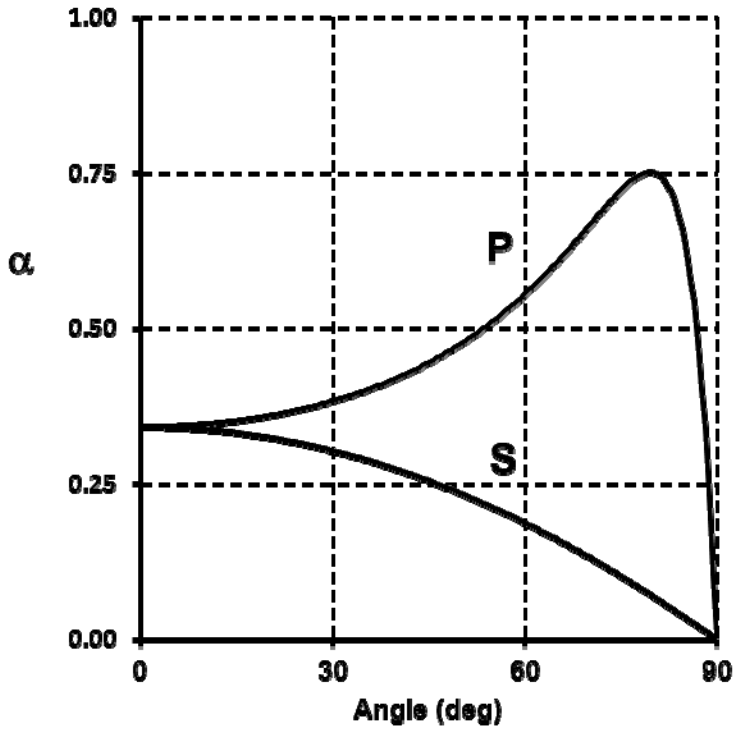

Fig. 1. Absorptivity α of 1 μm light incident on stainless steel.

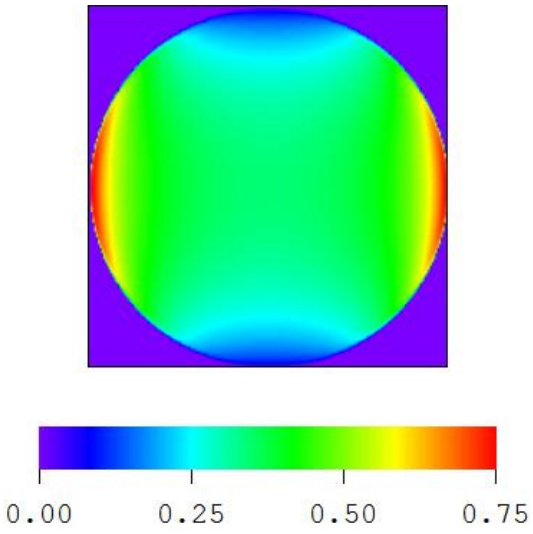

Fig. 2. Absorptivity α of a beam by a single sphere. The beam is polarized horizontally. The absorptivity falls to zero all along the edge, although this is not resolved in the graphic.

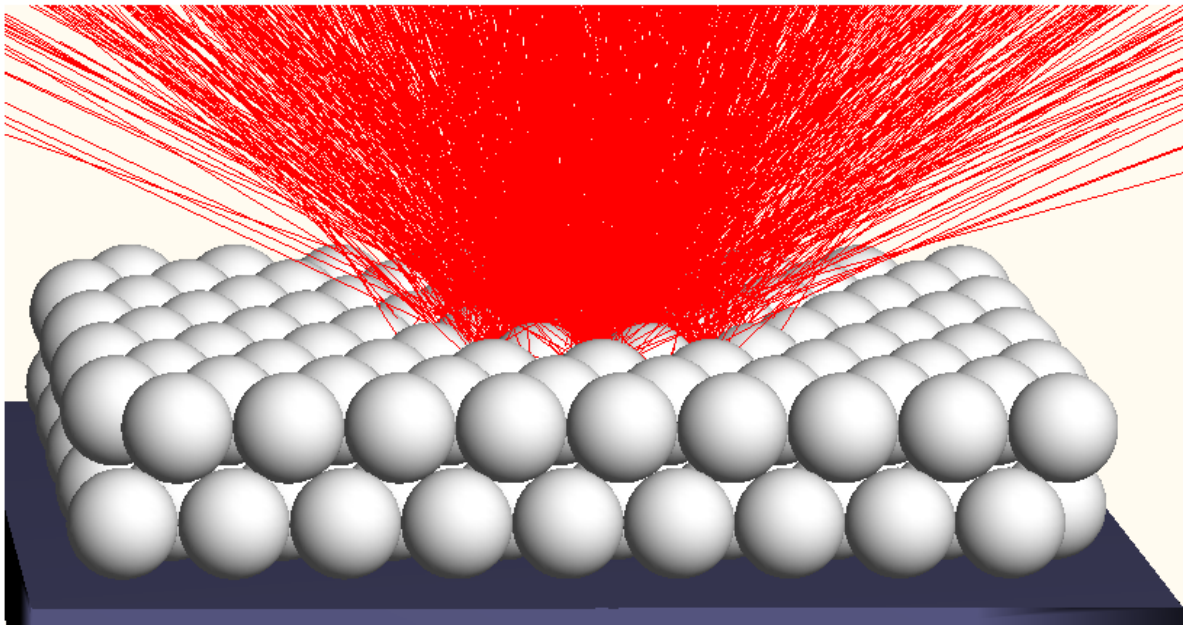

Fig. 3. Typical rays during illumination of the ideal array.

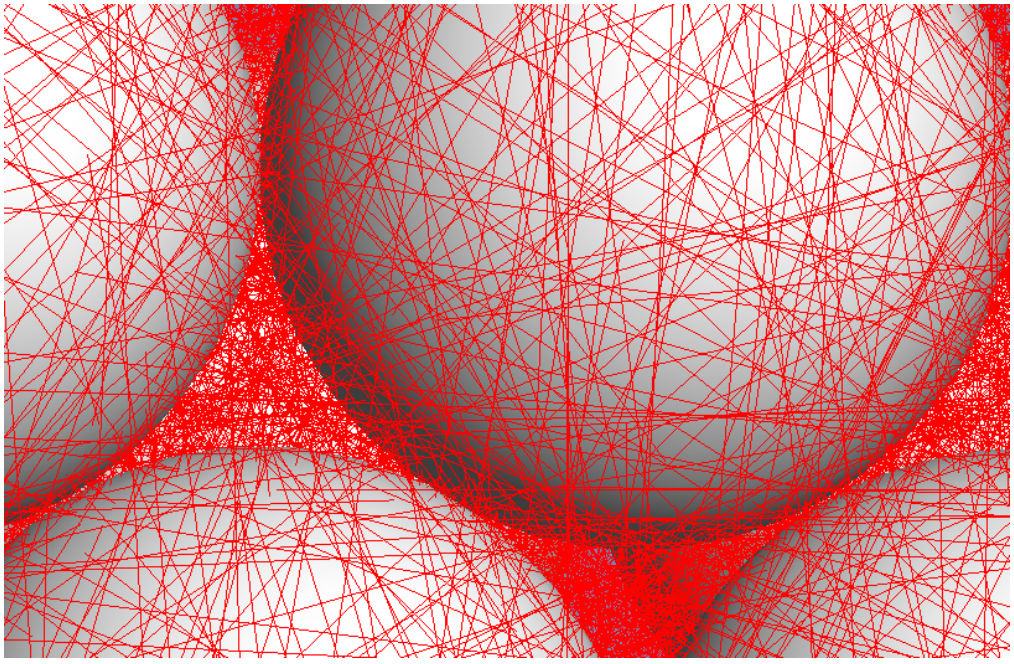

Fig. 4. Detail of ray trajectories in Fig. 3, showing multiple scattering from spheres.

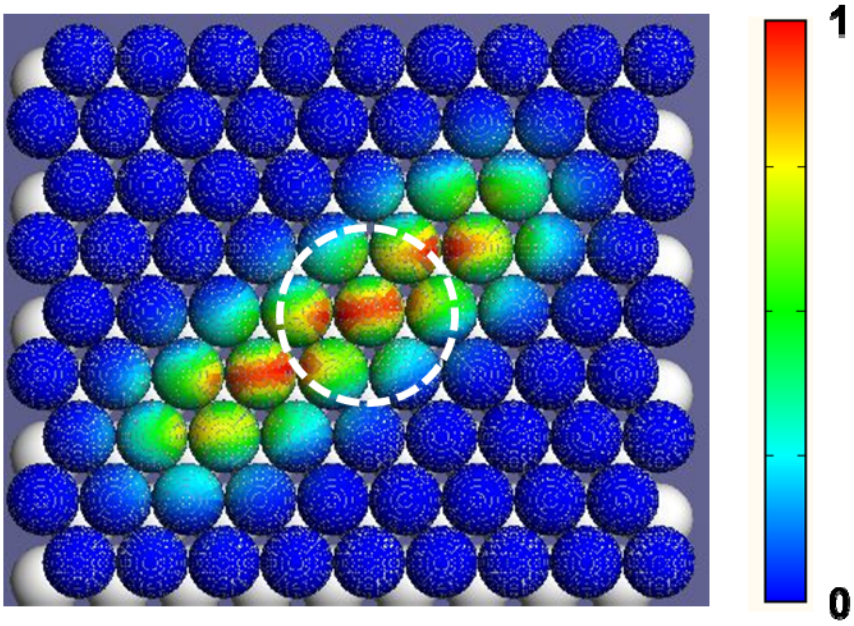

Fig. 5. Irradiances (arbitrary scale) for 61 successive beam positions, from lower left to upper right, in steps of 2 μm. The irradiances pertain to the spherical surfaces. A sample beam spot ($1/e^2$ radius) is shown.

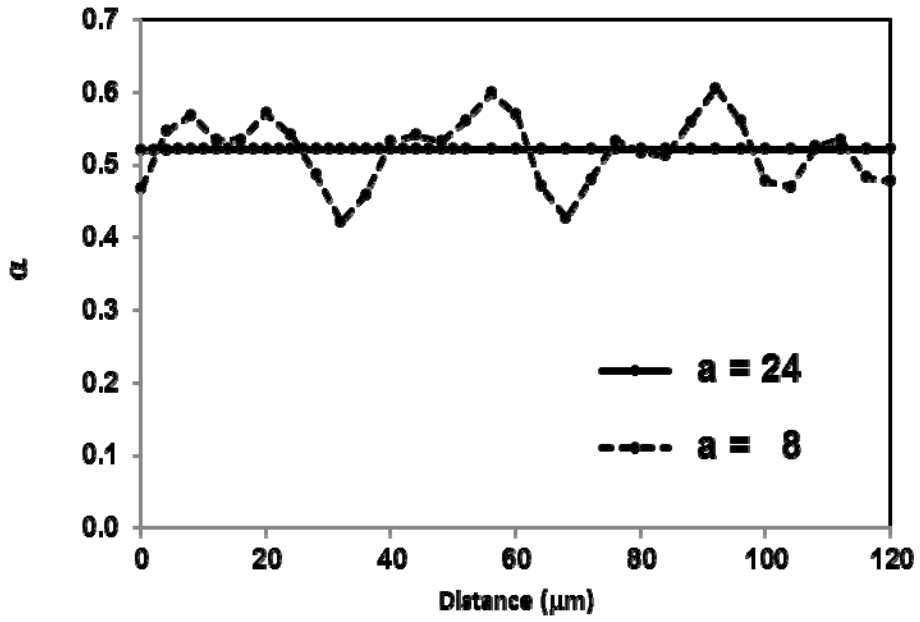

Fig. 6. Spatial variations of the absorption α along the beam path for beams of different radii.

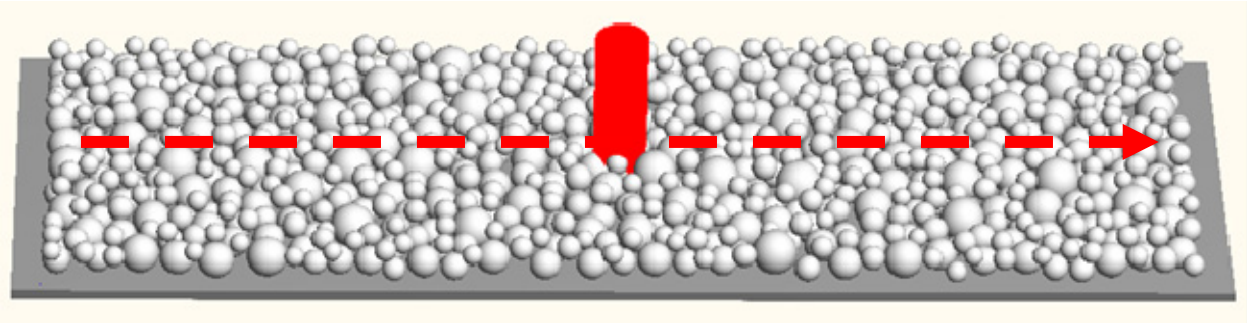

Fig. 7. Powder with a Gaussian distribution of sizes. The length of the bed is about 1100 µm, and the beam path is indicated.

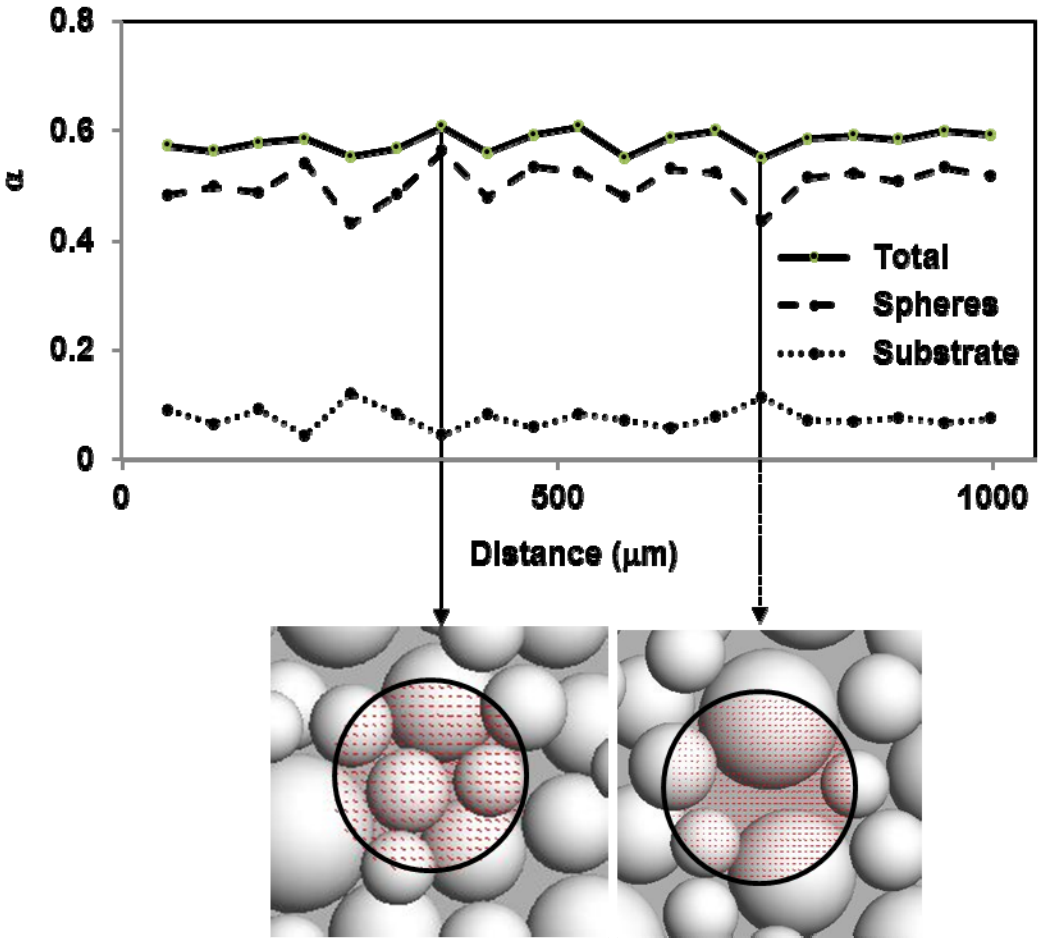

Fig. 8. Absorption α as calculated along the beam path for the Gaussian powder of Fig. 7. The material is stainless steel. The inserts show the powder and incident beam size ($1/e^2$) at locations with high absorption (left) and low absorption (right).

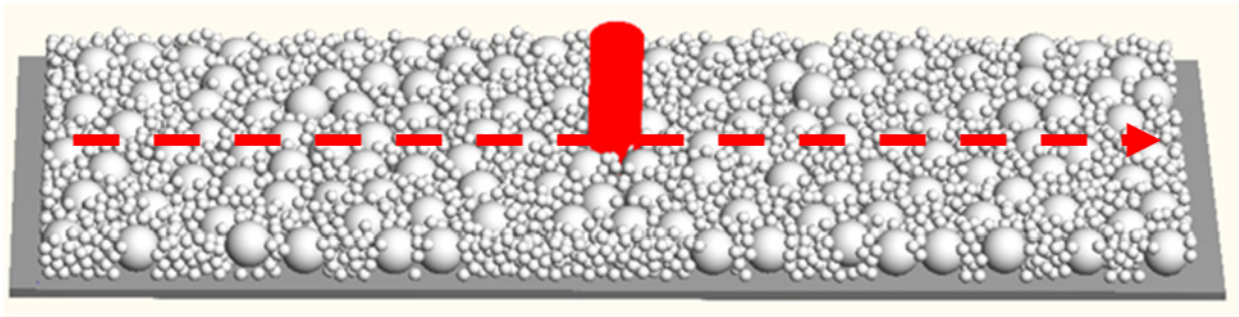

Fig. 9. Powder with a bimodal distribution of sizes. The powder bed and the beam are as in Fig. 7.

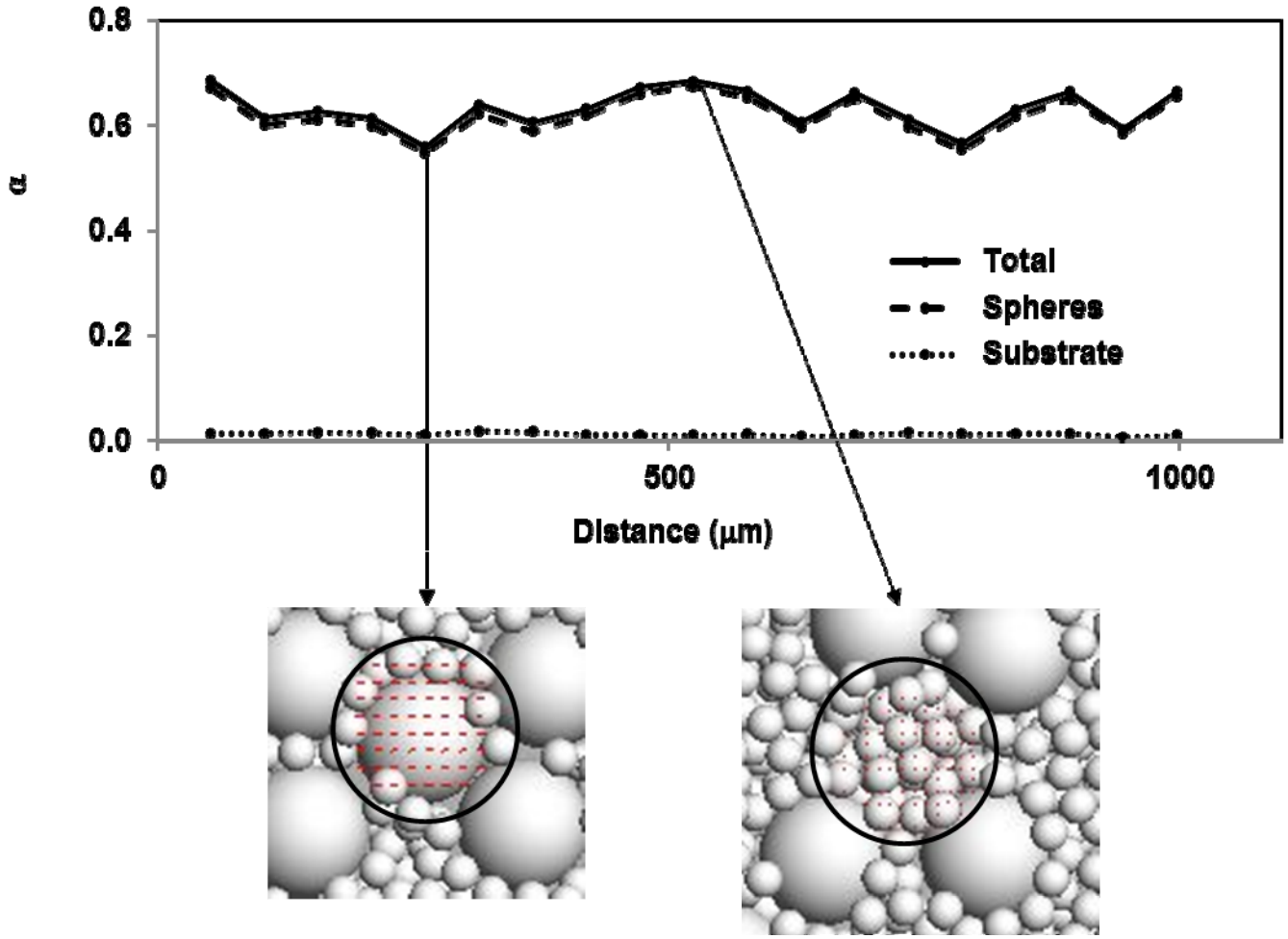

Fig. 10. Absorption α as calculated along the beam path for the bimodal powder of Fig. 9 (stainless steel). The inserts show the powder and incident beam size at locations with low absorption (left) and high absorption (right).